

# Proton Transfer and Photoluminescence Intermittency of Single Emitters in Dyed Crystals

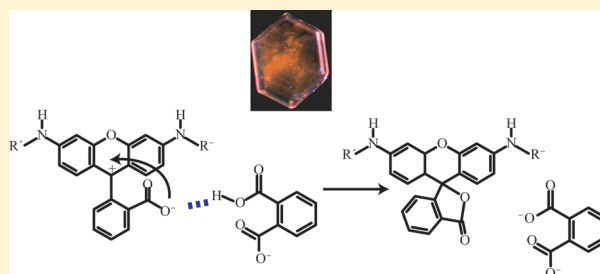
Erin A. Riley,<sup>†</sup> Chelsea M. Hess,<sup>†</sup> Jan Rey L. Pioquinto,<sup>†</sup> Werner Kaminsky,<sup>†</sup> Bart Kahr,<sup>\*,‡</sup> and Philip J. Reid<sup>\*,†</sup>

<sup>†</sup>Department of Chemistry, University of Washington, Box 351700, Seattle, Washington 98195, United States

<sup>‡</sup>Department of Chemistry, New York University, 100 Washington Square East, Room 1001, New York, New York 10003, United States

## S Supporting Information

**ABSTRACT:** The role of proton transfer in the photoluminescence intermittency (PI) of single molecules of violamine R (VR) overgrown in potassium acid phthalate (KAP) crystals is evaluated in comparisons of protonated (KAP) and deuterated (DKAP) mixed crystals between 23 and 60 °C. The PI is analyzed by the construction of cumulative distribution functions that are statistically compared. We find that the *on*- and *off*-interval duration distributions change with isotopic substitution consistent with proton transfer contributing to the PI of VR. The *on*- and *off*-interval duration distributions have distinct temperature dependencies consistent with different mechanisms for dark state production and decay. Additional evidence for proton-transfer is provided by distributions of single molecule emission-energy maxima that reflect emission from protonated and deprotonated VR. A mechanism for the PI of KAP is presented, where the dark state is assigned to formation of the colorless, leuco form of VR, formed by proton transfer from VR to the KAP lattice, and decay of the dark state involves ring-opening promoted by proton transfer from KAP to VR. The distributed kinetics for dark-state production and decay are modeled using a log-normal distribution for the PI data in preference to a power-law previously assumed. A discussion of the log-normal distribution with regards to PI and proton transfer is presented.



## ■ INTRODUCTION

The role of the surroundings or “host” in defining the photochemistry of a solute or “guest” is a long-standing area of study in condensed-phase chemical physics.<sup>1</sup> Anion vacancies (*farbe-* or *F*-centers) are classic sources of visible color in simple salts whose photophysical properties are determined by the surroundings.<sup>2</sup> More recently, we have studied the spectroscopic properties of “organic color centers”, complex dye molecules, in simple host crystals.<sup>3</sup> We have emphasized the photophysics of chromophores overgrown by, and oriented within, single crystals of potassium acid phthalate (KAP).<sup>4</sup> These adsorption phenomena appear to be highly specific as chromophores color particular growth sectors of KAP, or particular vicinal subsectors, depending on chromophore composition. Ensemble fluorescence anisotropy studies of dyed KAP crystals have established that the guest molecules are aligned during incorporation, however the details of chromophore incorporation remain unclear. In dyed crystals, forces operative in the docking and alignment of guest impurities, and their role in promoting or restricting the photochemical reactivity of the guest luminophore, can be systematically explored.<sup>5</sup>

Here, we report the photophysics of violamine R (VR), a rhodamine derivative, in KAP. VR is overgrown by the fast growing steps of the vicinal hillocks on the largest faces of KAP,

and oriented within the corresponding {010} growth subsectors. Initially, we established that single VR molecule orientations were more highly distributed than ensemble-averaged measurements indicated.<sup>6</sup> In addition, single molecule photoluminescence indicated that although the VR molecules were isolated in a solid matrix, the molecules exhibited emissive (*on*-intervals) and nonemissive (*off*-intervals) events lasting from milliseconds to minutes.<sup>7</sup> VR’s photoluminescence intermittency (PI) was consistent with distributed kinetics where the rate constants for dark-state production and decay evolve over the time scale of the measurement. Recently, we discovered that at elevated temperatures the average *on*- and *off*-interval duration increased for VR in KAP, yet a decrease in average duration time was observed for VR in films of poly(vinyl alcohol).<sup>8</sup> We proposed that the difference in temperature dependence was due to different operative pathways for dark state formation and decay in the two hosts. Specifically, in poly(vinyl alcohol), electron transfer was proposed to result in PI as for other rhodamine dyes in this

**Special Issue:** Paul F. Barbara Memorial Issue

**Received:** June 28, 2012

**Revised:** August 3, 2012

same host.<sup>8</sup> In contrast, the PI was proposed to result from proton transfer involving the hydrogen bonding network in KAP in which VR is incorporated.

In this work, the role of proton-transfer in promoting the PI of VR in KAP is investigated by isotopic substitution. Specifically, we compare the PI in KAP and deuterated KAP or DKAP. The distributions of *on*- and *off*-interval durations are analyzed using a new method based upon cumulative distribution functions (CDFs). We recently demonstrated that CDFs are superior for the comparison of the PI data because statistical comparisons can be employed to accept or reject the hypothesis that the two data sets arise from the same underlying probability distribution function.<sup>9</sup> Both the *on*- and *off*-intervals demonstrate sensitivity to isotopic substitution consistent with proton transfer as the origin of PI by VR in KAP. The *on*-interval duration distributions are only slightly affected by isotopic substitution or temperature whereas the *off*-interval distributions are strongly affected. This suggests that different proton-transfer mechanisms are responsible for dark-state production and decay. Statistical tests are employed to assess the validity of power-law distributed *on*- and *off*-interval durations previously assumed to describe the PI of VR in KAP.<sup>7,8,10</sup> The PI data are not consistent with a power law, but instead are best represented by a log-normal distribution. This method of testing alternate distributions and quantitatively comparing them provides a means for accurately determining the true PDF describing the data. The connection of log-normal distributed *on*- and *off*-events to the underlying VR photophysics responsible for PI is discussed.

## ■ EXPERIMENTAL SECTION

**Sample Preparation.** Violamine R (VR, Aldrich) was purified as described in the literature to 95% as determined by LC-MS.<sup>11</sup> Dyed crystals were grown by slow cooling growth solutions from 46 °C (H<sub>2</sub>O) and 48 °C (D<sub>2</sub>O) at 0.08 °C/hr in a customized water bath. Crystallization dishes were sealed and completely submerged to avoid condensation. Growth solutions were prepared by combining 14.3 g of KAP in 75 mL of nanopure water or D<sub>2</sub>O (Cambridge Isotopes). These solutions were brought to boiling, cooled slightly, and seeded. VR was then added to produce concentrations of  $\sim 10^{-8}$  M (D<sub>2</sub>O) and  $10^{-7}$  M (H<sub>2</sub>O), yielding defect-free crystals with VR concentrations appropriate for single molecule studies and  $\sim 10^{-5}$  M for heavily dyed crystals. Due to the reduced solubility of KAP in D<sub>2</sub>O, these crystals grew quickly (2.5 days vs 3.5 for those grown from H<sub>2</sub>O), resulting in an increase in dye incorporation.

**X-ray Crystallography.** Undoped crystals were characterized by X-ray crystallography. Two colorless prisms, measuring  $0.4 \times 0.3 \times 0.1$  mm<sup>3</sup> (KAP) and  $0.5 \times 0.4 \times 0.2$  mm<sup>3</sup> (DKAP) were mounted on glass capillaries with super glue. Data was collected at 296 and 360 K on a Bruker APEX II single crystal X-ray diffractometer. Crystal-to-detector distance was 40 mm and the exposure time was 10 s per frame for all sets with a scan width of  $0.5^\circ$ . Data collection was 99.9% complete to  $25^\circ$  in  $\theta$  covering a full sphere in the reciprocal lattice. The data was integrated and scaled using SAINT, SADABS within the APEX2 software package by Bruker.<sup>12</sup> Solution by direct methods (SHELXS, SIR97<sup>13,14</sup>) produced a complete heavy atom phasing model consistent with the known structure. The structure was refined by difference Fourier synthesis with SHELXL97.<sup>15,16</sup> Scattering factors are from Waasmair and Kirfel.<sup>17</sup> Hydrogen and deuterium atoms were

refined isotropically. All nonhydrogen atoms were refined anisotropically by full-matrix least-squares.

**Confocal Microscopy.** VR was photoexcited with a 532 nm laser (Spectra Physics Excelsior). The 3.2  $\mu$ W excitation intensity as measured at the entrance port to the microscope was polarized and aligned along the [001] crystallographic axis of the sample. The excitation field was focused onto the sample with a 1.3 NA objective (Nikon, Plan-Fluor), providing a diffraction-limited spot. Emission was collected in epi geometry, the excitation field was rejected with a 550 nm long-pass filter and focused onto a 70  $\mu$ m pinhole. The emission was split by a dichroic short pass mirror centered at 600 nm, with the reflected and transmitted light focused onto two separate avalanche photodiode detectors (Perkin-Elmer SPCM-AQR-16). Samples were mounted on a *xy*-piezoelectric scan stage (Physik Instrumente) outfitted with a custom sample heating stage employing two cartridge heaters (Omega CSS-01115) and a temperature controller (Omega CN 4321) providing stability to  $\pm 0.2$  °C. The following temperatures were used in experiments: ambient or 23, 45, and 60 °C, as measured at the point of contact between the crystal and objective. The top (010) surface of the crystals were removed by cleaving, and VR molecules  $\sim 3$   $\mu$ m into the crystal were investigated to avoid surface effects. Emission traces were collected using a 10 ms integration time and a total acquisition time of 5 min. Emission from SMs was judged on the basis of the diffraction-spot limited size of the fluorescence image, the complete extinction of fluorescence to the rms noise during *off*-intervals, and irreversible single-step photobleaching. The photoluminescence intermittency (PI) from VR in KAP was analyzed using the change point detection (CPD) algorithm applied to the sum of the two channels as described previously.<sup>10,18</sup> Deconvolved states with intensities greater than one standard deviation above the rms noise were designated as emissive or *on*. This definition of the emissive threshold designated the lowest deconvolved intensity state(s) as nonemissive or *off*. In addition to intensity transitions across this threshold, a molecule may move among emissive states of differing intensity. Therefore, we have analyzed the emissive events in two ways: first, in terms of the duration of a specific emissive intensity state, and second, in terms of the time that a molecule resides above or below the intensity threshold. As discussed previously, a fraction of VR molecules are continually emissive and are not included in the analysis herein except where noted. All data analysis was performed in Matlab (version 2011b). Data was collected from 64 individual molecules in each sample, with a minimum time to photodecomposition of 60 s.

**SM Emission Energies.** Spectral shifts were calculated using the variation in the reflected and transmitted light through a 600 nm short pass dichroic, with spectral calibration provided by the emission from dyed polystyrene beads. Ensemble spectra were convolved with the APD efficiency curves, the emission filter, the dichroic reflectance and transmission curves, and the polarization response of these curves. The dichroic ratio corresponding to the measured intensity of transmitted and reflected light from the dichroics was measured for heavily dyed crystals and verified at low excitation intensity to emulate the signal observed from single molecules. The ensemble VR KAP spectra were used to map shifts in fluorescence maxima into dichroic ratios (equal to the ratio of transmitted to reflected intensity from the dichroic) by shifting the spectra and convolving them with the response curves. The shifts greater than 200 cm<sup>-1</sup> are inaccurately

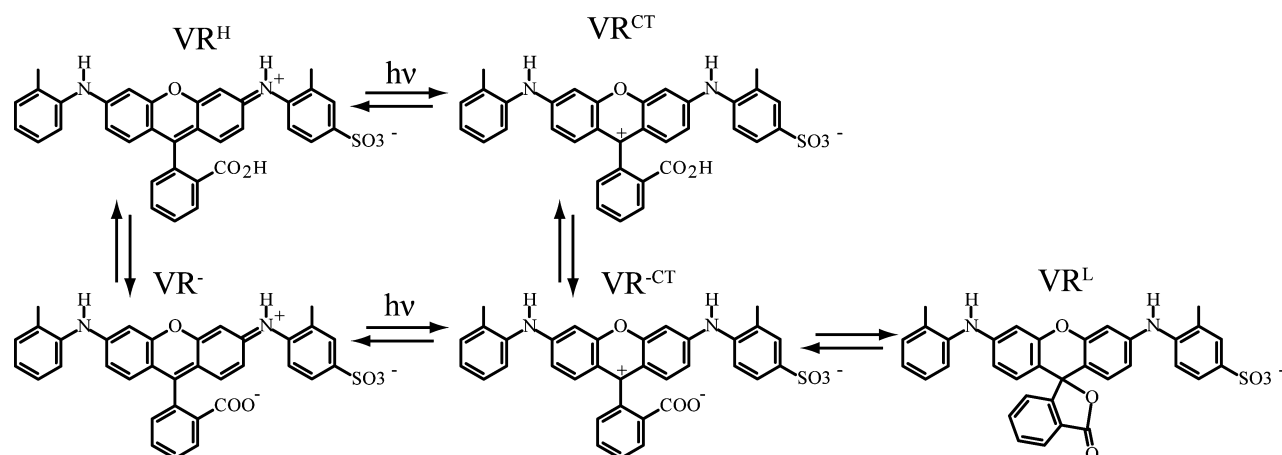


**Figure 1.** Scheme of possible VR protonation states and structures. In polar protic solvents,  $VR^H$  and  $VR^-$  are predominant. Photoinitiated charge transfer results in the formation of  $VR^{CT}$  and  $VR^{-CT}$ , with excited-state decay resulting in the reformation of  $VR^H/VR^-$ . In aprotic solvents, the dye is in the colorless or leuco form  $VR^L$ .

determined as the spectrum is cutout by the emission filter. Only emissive segments with durations  $>50$  ms were used in this analysis.

**Ensemble Spectroscopy.** Fluorescence spectra of heavily dyed crystals and VR solutions were obtained using a spectrometer (Horiba Fluorolog 3) equipped with a temperature-controlled flow cell with 1 nm spectral resolution and 532 nm excitation. Crystal absorbance spectra were recorded on a Varian Cary Eclipse 5000 spectrometer employing a pinhole mask. Solution absorbance spectra were recorded using a temperature controlled UV–vis spectrometer (Agilent 8453). A stock solution ( $3.3 \times 10^{-5}$  M) of violamine R (VR) was prepared in a 1 L volumetric flask by dissolving purified VR in 1 mL of ethanol and filling the flask with nanopure water (Barnstead, NANOpure II). KAP was added to achieve a buffer concentration of 50 mM. This stock solution was used to prepare solutions at pH 2.1 and 12.3 by adding concentrated HCl and sodium hydroxide pellets, respectively. Solutions at other pH values (2.1, 2.6, 3.0, 3.4, 4.15, 5.5, 6.9, and 8.7) were obtained by mixing acidic and basic solutions.

## RESULTS

**VR Ensemble Spectroscopy.** The photophysical properties of rhodamine dyes have been extensively studied.<sup>19–21</sup> The various protonated and zwitterionic forms of this compound are shown in Figure 1.<sup>11</sup> In protic solvents, VR is in a deprotonated zwitterionic state denoted as  $VR^-$ . The overall negative charge comes from the sulfonate group (only protonated under extremely acidic conditions not considered here). In mildly acidic conditions the protonated form of the chromophore ( $VR^H$ ) is dominant. When dissolved in acetone or other aprotic solvents, VR cyclizes to the colorless leuco form ( $VR^L$ ). The main nonradiative decay pathway for photoexcited  $VR^H$  and  $VR^-$  is fast intramolecular charge transfer to produce  $VR^{CT}$  and  $VR^{-CT}$ , respectively (Figure 1). The charge-transfer mechanism remains unclear. Both twisted intramolecular charge transfer (TICT) and evolution of the hybridization of the amino group from planar  $sp^2$  to pyramidal  $sp^3$  have been thought to promote charge transfer.<sup>20</sup> It has been shown that the charge on the sulfonate group, critical for VR solubility in water, remains localized and does not participate in charge transfer.<sup>22</sup> The excited state lifetime of VR is dependent on the hydrogen bonding ability of the solvent and also on the

protonation state of the arylcarboxy group that has an inductive effect on the xanthene moiety. In addition, hydrogen-bond accepting solvents stabilize the positive charge on the iminium group.<sup>19</sup> Finally, the quantum yield for triplet state formation of rhodamines is generally small. Moreover, the triplet state is thermally deactivated.<sup>11</sup>

The dependence of the absorption and emission of VR on protonation state and temperature was analyzed through ensemble absorption and fluorescence measurements in aqueous solution. The pH dependence of the absorption spectrum (Figure 2a) shows  $VR^H$  at pH 2. As the pH is

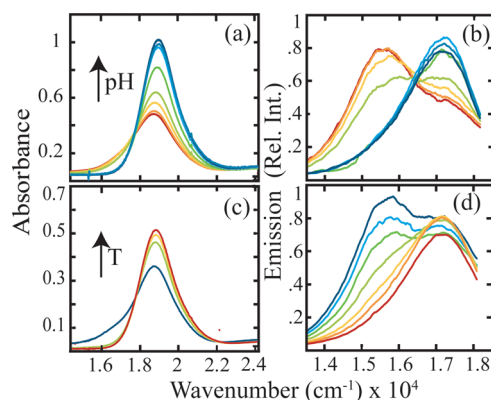


**Figure 2.** pH-dependent absorption (a) and emission (b) spectra of VR in aqueous solutions with KAP buffer concentration of 5 mM: pH 2.1, red; 2.6, orange; 3.0, yellow; 3.4, lime; 4.15, green; 5.5, teal; 6.9, blue; 8.7, dark blue. Temperature-dependent absorption (c) spectrum of pH 2.7 solution: temperatures of 25 °C, blue; 33 °C, green; 45 °C, yellow; 55 °C, red. Temperature-dependent emission transition from blue to red 23, 28, 32, 36, 40, 45, and 60 °C.

increased, a higher-energy absorption band becomes evident, consistent with  $VR^-$  ( $\nu_{\max} = 18900$   $\text{cm}^{-1}$ ), which is dominant by pH 6. The conversion of  $VR^H$  to  $VR^-$  with an increase in pH is consistent with the observation of an isosbestic point 15400  $\text{cm}^{-1}$  (Figure 2a). Subtraction of the pH 6 absorption spectrum from the pH 2 spectrum provides a crude estimate of the  $VR^H$  absorption maximum,  $\sim 17900$   $\text{cm}^{-1}$ , corresponding to a  $\sim 1000$   $\text{cm}^{-1}$  separation in the energy between  $VR^H$  and  $VR^-$  absorption maxima. The emission spectra (Figure 2b) are



also consistent with the conversion of  $\text{VR}^{\text{H}}$  and  $\text{VR}^-$  with an increase in pH. Specifically, at low pH emission from  $\text{VR}^{\text{H}}$  is observed with a maximum energy of  $15500\text{ cm}^{-1}$ , and as the pH is increased, emission from  $\text{VR}^-$  becomes evident with a maximum at  $17200\text{ cm}^{-1}$ . In contrast, only a  $300\text{ cm}^{-1}$  separation in emission maxima is observed in ethanolic solution, demonstrating that the hydrogen bonding nature of the surroundings greatly influences the fluorescence.<sup>11</sup> The  $\text{pK}_{\text{a}}$  of  $\text{VR}^{\text{H}}$  in water is estimated at  $\sim 3.2$ , where  $\text{VR}^{\text{H}}$  and  $\text{VR}^-$  concentrations are equal. The temperature-dependent absorbance spectrum for VR solution pH 2.7 is shown in Figure 2c. At room temperature the dye is predominately  $\text{VR}^{\text{H}}$ , and as the temperature is increased, the spectrum evolves to resemble  $\text{VR}^-$ . The change in the absorption spectrum with a relatively modest temperature increase from 25 to  $60\text{ }^{\circ}\text{C}$  suggests that the barrier to proton transfer between  $\text{VR}^{\text{H}}$  and the solvent is modest.

Figure 3 presents the absorbance and fluorescence spectra of VR in heavily dyed KAP and DKAP crystals grown at elevated

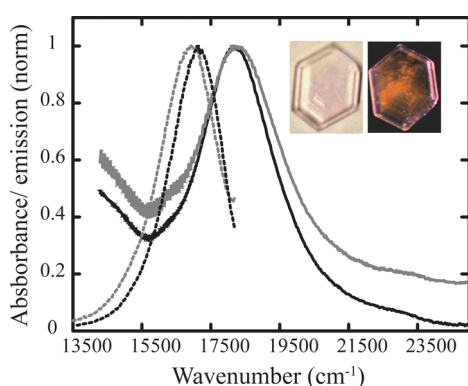


**Figure 3.** Absorption (solid) and emission (dashed) spectra of VR in KAP (black) and DKAP (gray) obtained with 532 nm excitation. Band maxima occur at  $\lambda_{\text{abs}} = 552\text{ nm}$ , and  $\lambda_{\text{fl}} = 583\text{ nm}$  for VR in KAP,  $\lambda_{\text{abs}} = 549\text{ nm}$ , and  $\lambda_{\text{fl}} = 591\text{ nm}$  for VR in DKAP. Inset: Heavily dyed VR KAP crystals are transparent in room light with a faint violet coloring (left), but fluoresce brilliantly under ultraviolet excitation (right). Dye in the  $\{010\}$  sector of the crystal (in the plane of the page) and more specifically contained in the fast growing slopes of the hillocks on these faces. For this reason, the coloration is not uniform.

temperature. The VR emission maxima are similar: DKAP ( $16900\text{ cm}^{-1}$ ) and KAP ( $17150\text{ cm}^{-1}$ ). This is remarkably different from crystals of KAP grown at room temperature ( $16260\text{ cm}^{-1}$ ). The emission spectra are consistent with comparable populations of  $\text{VR}^{\text{H}}$  and  $\text{VR}^-$  in KAP and DKAP grown at elevated temperature by slow cooling, with  $\text{VR}^-$  dominant in both crystals. Fluorescence spectra of VR dissolved in neutral  $\text{H}_2\text{O}$  and  $\text{D}_2\text{O}$  were likewise comparable; therefore, N–H vibrations do not impact spectral envelopes. The proposed mechanism of VR incorporation into KAP is substitution of the arylcarboxy moiety of VR for a hydrogen phthalate monomer directly into the hydrogen bond network of the KAP lattice.<sup>23</sup> The dimensions of the KAP and DKAP unit cells (Table 1) change with isotopic substitution. We note that a comparison of KAP and DKAP has been reported in the literature and it is in error.<sup>24</sup> While the  $a$  and  $b$  axes are larger in DKAP, the polar axis  $c$  is shorter due to the reduction in zero-point energy accompanying deuteration. The heavily dyed crystals of DKAP and KAP exhibit reduced fluorescence intensity with increased temperature but with the same

**Table 1.** KAP and DKAP Unit Cell and Thermal Expansion Coefficients<sup>a</sup>

KAP   DKAP	20 $^{\circ}\text{C}/\text{\AA}$	$\alpha_{\text{L}} (\times 10^{-5})/^{\circ}\text{C}^{-1}$
$a$	9.5955(2)   9.598(2)	3.375   2.861
$b$	13.2964(3)   13.320(3)	3.368   0.9188
$c$	6.46630(10)   6.4599(13)	4.916   6.238

<sup>a</sup>Expression for thermal expansion coefficient:  $\Delta L = \alpha_{\text{L}} \cdot L \cdot \Delta T$ .

energies. The protonation state of VR in KAP/DKAP is apparently not thermally activated.

**Single Molecule Spectroscopy.** Under continuous photoexcitation, single VR molecules in KAP exhibit emissive and nonemissive events, with the duration of these events ranging from milliseconds to minutes. Probability histograms of event durations qualitatively follow a power-law function of the form  $P(t) = At^{-\alpha}$  when viewed on log–log axes. We recently reported that the average *on*- and *off*-interval durations of VR in KAP increase with temperature as evidenced by a decrease in power-law exponent ( $\alpha$ ) with increasing temperature, and by comparing the mean values of the duration distributions.<sup>8</sup> The power-law analysis of the data was performed using the common method of constructing event duration histograms as shown in Figure 4a. This histogram is transformed into a continually decaying probability distribution function (PDF, Figure 4b) by dividing each entry in the histogram by the average time to the adjacent data points.<sup>25</sup> This process extrapolates the long-time tail of the distribution to produce a continuous probability distribution. The histogram data are then fit to a power-law for which a plot of  $\log(P(t))$  versus  $\log(t)$  should be linear. Overlaid on the histogram in Figure 4b is the best fit by a power-law using linear-least-squares regression. Although the fit appears reasonable, the data in Figure 4b are noisy, calling into question the reliability of the power-law exponent for comparing PI data sets. In addition, linear-least-squares regression provides an overestimation of the power-law exponent.<sup>26,27</sup> Our goal is to determine if isotopic exchange affects PI and the corresponding PDF, independently of correctly identifying the functional form of the PDF. Therefore, an alternative approach for analyzing PI data was employed to provide a statistical determination as to whether PI is affected by isotopic substitution.

The analysis of the PI data presented here relies on the comparison of cumulative distribution functions (CDF) defined as the probability of an event occurring in a time less than or equal to  $t$ . The CDF is related to the integral of the PDF:

$$S(t) = \int_{t_{\min}}^t P(\tau) d\tau \quad (1)$$

In the above expression  $S(t)$  is the CDF and  $P(\tau)$  is the corresponding PDF. The CDF is bound by zero when  $t < t_{\min}$ , and one at the longest observation time.  $S(t)$  can be computed directly from PI data from the correspondence between integrals and sums:

$$S(t) = \frac{1}{N} \sum_i t_i < t \quad (2)$$

In the above expression,  $t_i$  is an event duration less than time  $t$ , and  $N$  is the number of events. This distribution is zero for all times less than the shortest event (or time resolution) and one for all times greater than the longest event in the sum. The complementary CDF is given by

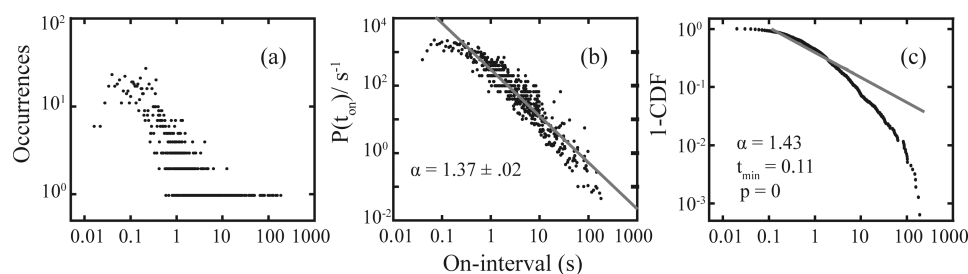


**Figure 4.** VR-KAP *on*-interval data displayed three ways. (a) A histogram of the raw data. The minimum time, 10 ms, corresponds to the experimental bin time. (b) The same histogram smoothed by dividing by the average time between nearest neighbors. Overlaid is the linear least-squares fit corresponding to a power-law distribution. The value  $\alpha$  corresponds to the power-law coefficient, with the error representing one standard deviation. Data appear to follow a power-law distribution, but deviations are evident at earliest and latest times. (c) The complementary cumulative distribution function (1-CDF) derived from the raw data in Figure 1a. The figure shows substantial curvature in a log–log plot of the CDF inconsistent with a power-law distribution. Best fit to the data by a power-law also illustrates the rejection of the power-law hypothesis with a *p*-value of zero.

$$F(t) = 1 - S(t) \quad (3)$$

$F(t)$  is the probability of observing an event at a time greater than  $t$  and is useful for visualizing PI data because the event probabilities are greatest at short times.

The complementary CDF obtained from the data in Figure 4a is shown in Figure 4c. The CDF, a straightforward measure of the evolution in probability density with time, is calculated directly from the data (no extrapolation between data points is required). For instance, the CDF in Figure 4c shows that the probability of *on*-intervals greater than 10 s is 10% and greater than 100 s is 1%. The CDF provides a direct way to determine the underlying PDF because the two are related by an integral. Using a power law as an example, the integral of a power law is also a power law. Therefore, the CDF derived from a power law PDF should be linear on a log–log plot. Surprisingly, the curvature evident in Figure 4c indicates that the data is *not* consistent with a power-law PDF. We have previously presented the formalism for fitting PI data to a variety of potential PDFs, this approach includes a hypothesis test using *p*-values corresponding to the probability that the data are derived from a specific PDF.<sup>9</sup> For example, testing the power-law hypothesis developed through analyses, as in Figure 4b, required calculating the best fit parameters for a power-law function. The CDF of the power-law fit is overlaid on the CDF of the data in Figure 4c, showing that the straight line poorly fits the data. The calculated probability (*p*-value) for the power-law PDF as the underlying distribution for these data is zero demonstrating that the PI data are not consistent statistically with a power-law PDF.

CDFs are also employed in a statistical method called the Kolmogorov–Smirnov (KS) test that provides a method for determining if two data sets correspond to the same PDF.<sup>28</sup> The central idea behind this test is that if data sets are generated from the same PDF, then the CDF's of the two data sets should overlap. The degree to which two CDFs overlap is quantified by calculating the maximum deflection ( $D$ ) between the two CDFs:

$$D = \max_{-\infty < t < \infty} |S_1(t) - S_2(t)| \quad (4)$$

In the above equation,  $D$  is distributed according to another PDF, the Kolmogorov–Smirnov (KS) distribution. The KS distribution is important for application of the statistical test, however, the KS distribution never explicitly enters into the test. Instead, the CDF of the KS distribution is determined and used to calculate a *p*-value for a given  $D$  determined from the

CDFs of two different data sets. To quantify the differences observed between the two CDFs, the *p*-value is computed from the CDF of the KS distribution,  $S_{KS}$ . The CDF is used because all points in the CDF correspond to an integrated area of the PDF providing the probability of a measured  $D$  value. The *p*-value is calculated as follows:

$$p\text{-value} = 1 - S_{KS}([\sqrt{N_e} + 0.12 + 0.11/\sqrt{N_e}]D) \quad (5)$$

where  $S_{KS}$  is given by<sup>28</sup>

$$S_{KS}(z) = \sqrt{\frac{2\pi}{z}} \sum_{j=1}^{\infty} \exp\left(\frac{-(2j-1)^2\pi^2}{8z^2}\right) \quad (6)$$

Additionally,  $N_e = N_1N_2/(N_1 + N_2)$  is the reduced data density that accounts for differences in the number of data points for the two CDFs. This analysis was employed to compare CDFs obtained for VR in KAP and DKAP and at three temperatures in both crystals (23, 45, and 60 °C). The results of this analysis are presented in Figure 5. Figure 5a shows a comparison of the *on*-interval CDFs for VR in KAP and DKAP with corresponding *p*-values calculated for each temperature. For reference, *p*-values > 0.05 mean that the data have a greater than 5% probability of being derived from the same PDF. The analysis presented here demonstrates that the *on*-interval data in KAP and DKAP are statistically different at room temperature (*p*-value of  $10^{-15}$ ) but become statistically equivalent at elevated temperature (*p*-values > 75%). In contrast, the *off*-interval data (Figure 5b) for VR in KAP versus DKAP are statistically different at all temperatures. We note that the average *on*- and *off*-interval durations for VR in DKAP increase with an increase in temperature. In contrast, for VR in KAP average duration times increase as the temperature is raised from 23 to 45 °C, but then decrease from 45 to 60 °C. The *on*-segment data (Figure 5c), defined as the duration of individual intermediate intensity states above the emissive threshold, show that the PI of VR in KAP and DKAP remain statistically different up to 60 °C.

**Fitting CDFs.** Three potential PDFs (power law, Weibull, and log-normal) were fit to the PI data with details of the fitting procedure provided elsewhere.<sup>9</sup> Briefly, maximum log-likelihood estimation was used to determine the best-fit PDF parameters, and synthetic data sets were then generated using these parameters to determine the probability that the experimental data correspond to the same PDF as measured by the *p*-value. The log-normal distribution provided the largest

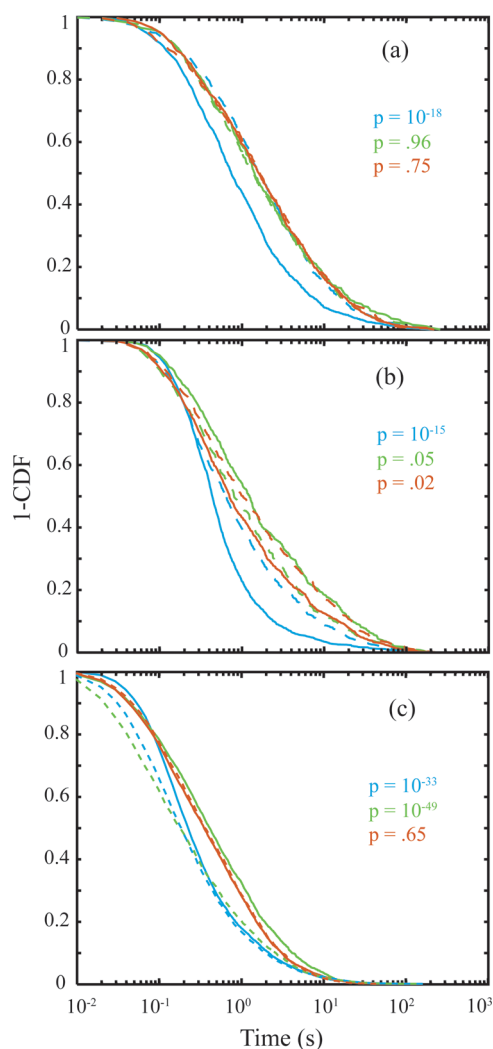


**Figure 5.** CDFs of *on* (a) and *off* (b) intervals and *on*-segments (c) for VR in KAP and DKAP at all three temperatures. *On*-segments are the durations of individual intermediate intensity states above the threshold, whereas intervals denote the total time the molecule's emission is above (*on*) or below (*off*) the threshold. Dashed lines are DKAP and solid lines are KAP at room temperature (blue), 45 °C (green), and 60 °C (red). The *p*-values correspond to the comparison of the CDFs for DKAP and KAP at the same temperature. *p*-values > 0.05 indicate that the data may arise from the same underlying probability distribution.

*p*-values corresponding to the best representation of the data. However, the *on*-interval data are the only data that are strongly log-normal with *p*-values approaching unity. The log-normal fit to 23 °C DKAP data is shown in Figure 6a. To test the fit, *p*-values were calculated (eq 5) comparing the CDF of the fit to the CDFs of the elevated temperature data and were >0.22, consistent with all *on*-interval DKAP data corresponding to the same log-normal PDF. The log-normal PDF is presented in Figure 6b. The log–log representation shows that the PDF has a slight curvature that could easily be obscured in a log–log plot, as shown in Figure 4b. The standard log-normal distribution and corresponding CDF are given by<sup>29</sup>

$$P(t) = \frac{1}{\sqrt{2\pi}\sigma t} e^{\left(-\frac{1}{2}\left[\frac{\log(t)-\mu}{\sigma}\right]^2\right)}, \quad t > 0 \quad (7)$$

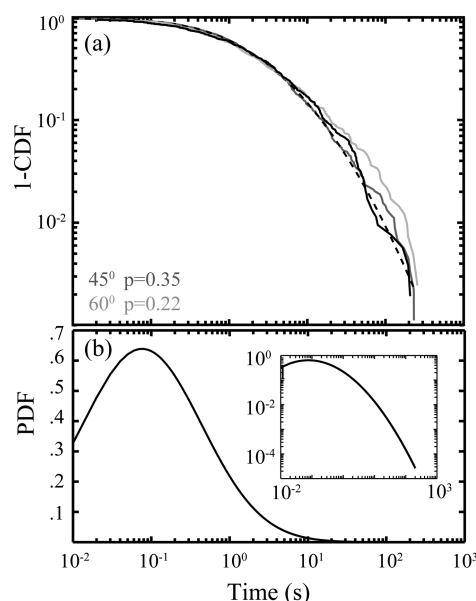


**Figure 6.** (a) *On*-intervals for VR in DKAP are shown in solid for the three temperatures. Room temperature data fit to a log-normal distribution (dashed black). *p*-values > 0.05 are consistent with the data corresponding to the same distribution. The data are best fit by a log-normal distribution. (b) Log-normal PDF for the best fit to the data shown on semilog axes and log–log axes (inset). Fit parameters for individual data sets are given in Table 2.

$$S(t) = \frac{1}{2} \operatorname{erfc}\left(-\frac{1}{\sqrt{2}}\left[\frac{\log(t)-\mu}{\sigma}\right]\right) \quad (8)$$

With the first moments of the distribution given by

$$\text{mean} = e^{\mu+\sigma^2/2} \quad (9)$$

$$\text{std dev} = \text{mean} \cdot \sqrt{e^{\sigma^2} - 1} \quad (10)$$

$$\text{median} = e^{\mu} \quad (11)$$

In these expressions,  $\mu$  is the mean and  $\sigma$  the standard deviation of the variable's natural logarithm, that is,  $\mu = 1/N \sum_i \ln(t_i)$ . The log-normal distribution occurs when the logarithm of the sampled variable is Gaussian distributed, as shown in Figure 6b, with the semilog plot of the PDF revealing the Gaussian functional form.

The properties of the log-normal CDF can be used to assist in the interpretation of the PI data in terms of changes in the skewness and median of the PDF, as shown in Figure 7. With a change in  $\sigma$ , the skewness of the distribution is altered, resulting in a change in the shape of the corresponding CDF, but the median is preserved. When  $\mu$  is changed the CDF's are horizontally shifted from one another (the skewness is unaltered), but the median is changed. Notice that maximum value or mode of the PDF is dominated by  $\sigma$  in the regime where  $\sigma$  is greater than 1. The arrows in Figure 7b show the locations of the mean which is far from the mode of the PDF. The values of  $\mu$  and  $\sigma$  obtained from fitting the *on*- and *off*-interval data are given in Table 2, with 95% error reported. The table shows that the values for  $\sigma$  are generally similar within error, and the most statistically significant changes are manifest in the parameter  $\mu$ .

Figure 8a,b presents best fits for the *off*-interval CDFs to log-normal PDFs. Other PDFs were investigated; however, similar

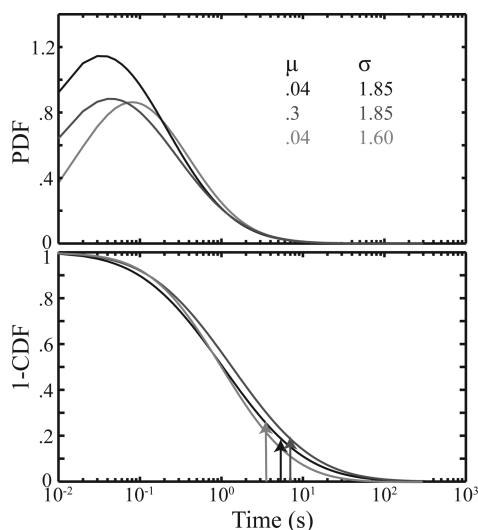


**Figure 7.** Depiction of the change in log-normal PDF and CDF with  $\mu$  and  $\sigma$ . Changes in  $\sigma$  result in a shift in maximum probability for the PDF, a crossing of CDFs at 0.5. Changes in  $\mu$  result in horizontal shifts along the  $x$ -axis. Arrows indicate the mean values that appear in the tail.

to the results for *on*-intervals, the log-normal most closely represents the data evidenced by several  $p$ -values  $> 10^{-4}$  versus 0 for other distributions. *Off*-intervals show horizontal shifts of the CDF's indicating similar skewness of the distribution. Different data sets were characterized by changes in the median. Figure 8 also demonstrates that the *on*-segments are not well represented by a log-normal PDF at any temperature, with very few calculable  $p$ -values. Though the visual fit is better than for *off*-intervals, the  $\sim 5$  times greater *on*-segment data density requires much smaller values of  $D$  to pass the hypothesis test. This indicates a different underlying distribution altogether is responsible for changes in emissive states of differing intensity. As described above, crossings of the CDFs indicate changes in the skewness of the underlying distributions. Both KAP and DKAP show crossings in the tail of the CDF at all temperatures in the segment data.

**Single Molecule Emission Energies.** The emission energies for single VR molecules in KAP and DKAP were measured to investigate photoinitiated exchange between  $\text{VR}^-$  and  $\text{VR}^{\text{H}}$ . As described above, a dichroic mirror separated the emission into two spectral windows: 550–600 and  $>600$  nm. A representative fluorescence trace of intensity for each spectral component with time for VR in DKAP is shown in Figure 9a and b for 10 and 100 ms time bins, respectively. The ratio of the two channel intensities (Figure 9c) shows correlated fluctuations where increased intensity is observed for both

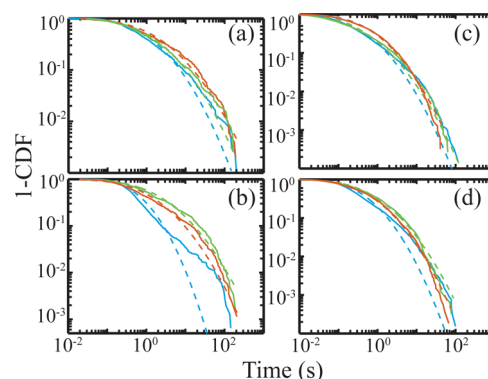


**Figure 8.** Log-normal fits (dashed lines) to CDFs for each temperature, blue 23 °C, green 45 °C, and red 60 °C, for *off*-intervals of DKAP (a) and KAP (b). As temperature is increased, the data become more consistent with log-normal distributions. Emissive segments for DKAP (c) and KAP (d) show poor fits to a log-normal PDF. Additionally, on log–log axes, crossings of the CDF are observed at long times, suggesting changes in the width of the underlying PDF with temperature.

spectral components of the emission. If these fluctuations were due to spectral diffusion alone, then the intensities would be anticorrelated. The correlated changes in fluorescence intensity are consistent with proton transfer from  $\text{VR}^{\text{H}}$  to  $\text{VR}^-$ . Specifically, the larger molar absorptivity of  $\text{VR}^-$  combined with the similarity in emissive intensity between  $\text{VR}^{\text{H}}$  and  $\text{VR}^-$  revealed by the solution-phase spectroscopy (Figure 3) suggests that an increase in emissive intensity and change in the spectral intensity ratio should both be observed, as is evident in Figure 9.

The spectral shifts observed for single VR molecules in KAP and DKAP are presented in Figure 10. Emission energies were calculated, as described in the Experimental Section, with segment durations and intensities used to calculate the photon weighted energy shift. The average emission energies are consistent with ensemble spectra. The data presented in Figure 10 demonstrate that a substantial number of emission events occur at lower energy, consistent with emission from  $\text{VR}^{\text{H}}$  obtained in ensemble measurements presented in Figure 2. In addition, room-temperature grown VR KAP crystals exhibit a  $-900 \text{ cm}^{-1}$  shift in emission energy relative to the VR KAP crystals grown at elevated temperature consistent with  $\text{VR}^{\text{H}}$  as the dominant species in room-temperature grown crystals.

## DISCUSSION

The prevailing hypothesis for organic luminophore PI is intermolecular electron transfer to the surrounding environment.<sup>1</sup> The distribution of electron trapping sites surrounding

**Table 2.** Log-Normal Parameters for *On*- and *Off*-Intervals<sup>a</sup>

		$\mu$		$\sigma$	
		<i>on</i>	<i>off</i>	<i>on</i>	<i>off</i>
23 °C	KAP	$-0.13 \pm 0.08$	$-0.63 \pm 0.064$	$1.63 \pm 0.06$	$1.28 \pm 0.047$
	DKAP	$0.5 \pm 0.1$	$-0.2 \pm 0.1$	$1.76 \pm 0.085$	$1.7 \pm 0.16$
45 °C	KAP	$0.44 \pm 0.14$	$0.42 \pm 0.15$	$1.81 \pm 0.1$	$1.87 \pm 0.1$
	DKAP	$0.5 \pm 0.2$	$0.04 \pm 0.2$	$1.87 \pm 0.14$	$1.8 \pm 0.14$
60 °C	KAP	$0.5 \pm 0.1$	$-0.02 \pm 0.1$	$1.76 \pm 0.085$	$1.81 \pm 0.08$
	DKAP	$0.5 \pm 0.16$	$0.3 \pm 0.17$	$1.85 \pm 0.1$	$1.9 \pm 0.1$

<sup>a</sup>Errors represent 95% error.



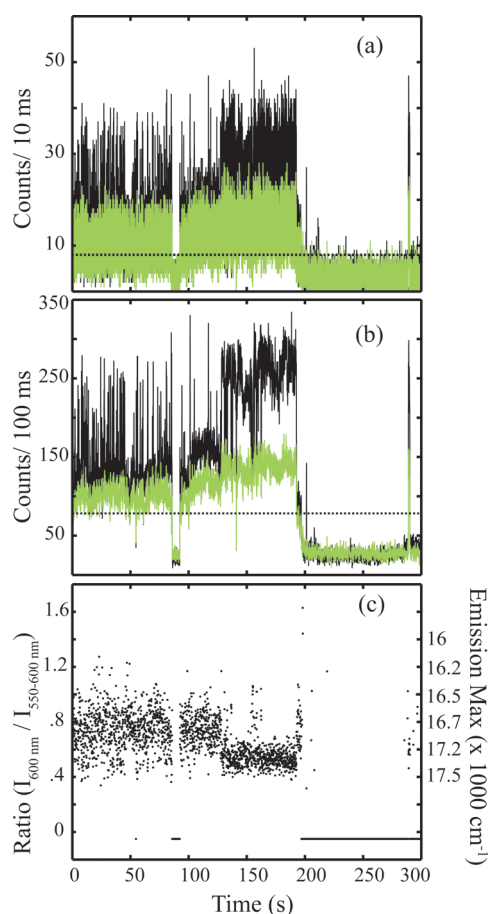


**Figure 9.** Emission trace of VR in DKAP showing evolution in the protonation state of the molecule. (a) Data presented using at 10 ms bin time. Green corresponds to emission wavelengths >600 nm and black from 550 to 600 nm. Emissive threshold is represented by the horizontal dotted line. (b) Data presented using a 100 ms bin time. (c) Ratio of the two dichroic components ( $I_{600\text{nm}}/I_{550-600\text{nm}}$ ). Approximate emission energy corresponding to the ratio axis given in gray. Ratio of 0.7 corresponds to heavily dyed DKAP emission maximum. An increase in emission intensity is observed corresponding to a lower ratio (higher emission energy) of the two detectors consistent with the proton transfer resulting in the formation of  $\text{VR}^-$ .

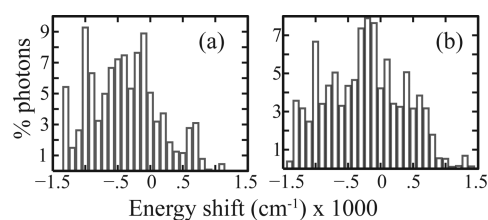


**Figure 10.** Energy shift histograms for VR in KAP (a) and DKAP (b). Histogram represents the fraction of photons collected for each emission maximum relative to heavily dyed KAP (zero on the x-axis for both panels). The emission from heavily dyed DKAP is shifted  $-260\text{ cm}^{-1}$  relative to KAP. The observation of energy shifts  $\sim -900\text{ cm}^{-1}$  is consistent with  $\text{VR}^{\text{H}}$  formation.

the luminophore presumably results in a distribution of electron transfer rates that is responsible for dispersed kinetics and the corresponding power-law distributed *on*- and *off*-interval durations. Tests of this hypothesis have involved the restriction or elimination of trapping sites resulting in (often modest) changes in the power-law coefficient. However, the

electron transfer mechanism need not be universal. For example, one-dimensional diffusional electron transfer models predict that the power-law coefficient should be 1.5, yet power-law coefficients as low as 1 and as high as 2 have been reported.<sup>30,31</sup> Marcus and Tang advanced a model combining these concepts called diffusion controlled electron transfer.<sup>32</sup> This model successfully incorporates most ancillary observations such as spectral diffusion and exponential fall off in the tails of some power-law distributed PI data. The luminophore's surroundings also influence photophysical processes such as conformational flexibility,<sup>33-35</sup> spectral diffusion,<sup>32,36-38</sup> proton transfer,<sup>39,40</sup> intramolecular electron transfer,<sup>41,42</sup> and electron transfer<sup>43-46</sup> all of which affect PI. Determining which of these mechanisms are operative represents a significant challenge in any PI study. Finally, it is often difficult to make statistically sound comparisons between duration histograms based on power-law exponents alone given the degree of dispersion of the data around the power-law fit as presented earlier (Figure 4).

Previously, we employed power-law exponents as a way to quantify the PI of VR in KAP. However, the absence of statistical tests with which to measure the change in PI with external perturbation (temperature, isotopic substitution, etc.) significantly limited the conclusions of these earlier studies. In contrast, the analysis here compares duration histograms without having to first assume the identity of the underlying PDF. The CDFs derived from two data sets are quantitatively compared using the KS test which returns the probability that the data arise from the same underlying PDF. The advantages of this new analysis were evident in Figure 4 where it was shown that the PI data do not conform to a power-law. As such, the comparison of power-law coefficients for isotopic perturbations are groundless. In contrast, the CDF analysis provides a clear statistical test of the effect of system perturbation on PI data.

**Proton Transfer and PI.** The results presented here support the hypothesis that proton-transfer is responsible for PI of VR in KAP. First, if proton-transfer is operative then isotopic substitution should have a measurable effect on PI, and the analysis presented above demonstrates that isotopic substitution alter VR blinking with statistical significance. At room temperature the CDF's for both the *on*- and *off*-intervals are statistically different for VR in KAP versus DKAP as evidenced by  $p$ -values  $< 10^{-15}$  (Figure 5). With an increase in temperature, the differences between the *on*- and *off*-interval CDFs in KAP and DKAP decrease and effectively vanish for the *on*-intervals, as evidenced by  $p$ -values approaching one. This difference in temperature dependence for the *on*- and *off*-intervals suggests that the proton-transfer energetics are different for production and decay of the dark state populated during nonemissive events. Further support for the proton transfer mechanism is found in the measurements of SM emission energies. Ensemble measurements of VR emission as a function of pH demonstrate that a spectral shift should accompany a change in protonation state from  $\text{VR}^{\text{H}}$  to  $\text{VR}^-$  (and vice versa). SM studies were performed to measure changes in emission energies, and fluctuations were consistent with proton transfer (Figure 10). Specifically, correlations between dichroic ratio as well as changes in overall emissive intensity (Figure 9) were consistent with exchange between  $\text{VR}^{\text{H}}$  and  $\text{VR}^-$ .

We previously proposed that the arylcarboxyl moiety of VR substitutes into the KAP lattice by replacing a hydrogen phthalate monomer.<sup>23</sup> The unit cell of KAP is shown in Figure



11b viewed along the  $c$  axis. The structure of KAP consists of layered sheets of hydrogen phthalate monomers hydrogen

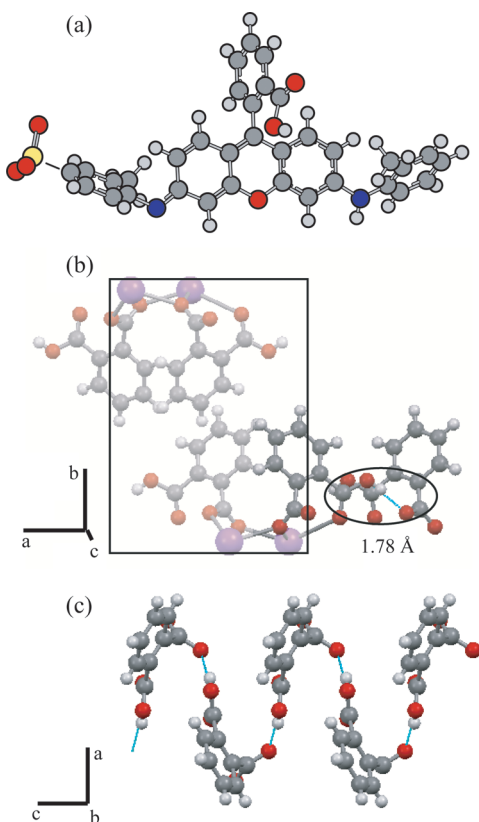


**Figure 11.** (a) Structure of VR. (b) Illustration of the unit cell of KAP projected on the  $ab$  plane. Hydrogen bonding occurs between adjacent monomers along the polar  $c$  axis. (c) Projection of one extended layer of phthalate monomers in the  $ac$  plane with potassium ions removed illustrating the hydrogen bond network in KAP (rings point out of page). Hydrogen bonds are indicated by blue lines. VR incorporates into the  $\{010\}$  sector of the crystal by direct substitution of the arylcarboxylate moiety into this hydrogen bond network during crystal growth.

bonded in a herringbone structure, as illustrated in Figure 11. The hydrogen bond network only extends down the  $c$  axis of the crystal, and is responsible for the piezoelectric effect in KAP. The AC conductivity of KAP is consistent with an activation energy of 0.022 eV at 1 kHz, a low barrier for charge carrier hopping.<sup>47</sup> If VR is incorporated into KAP through the arylcarboxyl moiety substituting for a phthalate in this network, a proton will be shared between the hydrogen phthalate and VR through a hydrogen bond.

We propose the following model for proton transfer and PI, illustrated in Figure 12. First,  $\text{VR}^-$  is the dominant species in KAP and DKAP. This species undergoes frequent proton exchange with KAP, as evidenced by changes in emissive intensity and shifts in the emission spectrum (step I in Figure 12). Facile proton exchange between  $\text{VR}^-$  and KAP is supported by the temperature dependence of the absorbance spectra where a substantial shift in protonation state is observed with a modest change in temperature consistent with a small barrier to proton transfer (Figure 2c). Next, photoexcitation results in the formation of  $\text{VR}^{-\text{CT}}$  (step II in Figure 12). This species can either relax to the ground electronic state, or undergo a ring-closure reaction resulting in the formation of

$\text{VR}^{\text{L}}$  (steps III and IV in Figure 12). Because this later species is colorless, the formation of  $\text{VR}^{\text{L}}$  corresponds to the nonemissive events in the PI data. The migration of the proton on the neighboring phthalate into the KAP lattice then stabilizes  $\text{VR}^{\text{L}}$  (step III in Figure 12). The leuco form is dominant in nonhydrogen bonding solvents, and ring-opening occurs in solvents capable of hydrogen bonding. Subsequent protonation of the phthalate monomer promotes the conversion of  $\text{VR}^{\text{L}}$  to  $\text{VR}^-$  (steps V and VI in Figure 12). The results presented above demonstrate that the average off-interval duration increases with temperature such that the conversion of  $\text{VR}^{\text{L}}$  to  $\text{VR}^-$  is not a thermally activated process. Instead, these results point to a proton-tunneling path to the reformation of  $\text{VR}^-$ . Support for proton tunneling is found in the change in unit-cell dimensions for KAP and DKAP with temperature (Table 1). The data show that the hydrogen bond distance in KAP is shorter than in DKAP ( $\text{O}\cdots\text{O}$  distances of 2.547(2) Å in KAP and 2.563(2) Å in DKAP) with only modest change with temperature (at 87 °C, 2.552(2) in KAP and 2.566(4) in DKAP). The change in  $\text{O}\cdots\text{O}$  distances compared favorably with differences between  $\text{KH}_2\text{PO}_4$  and  $\text{KD}_2\text{PO}_4$ .<sup>48</sup> Increased hydrogen bond length and distances to neighboring hydrogen phthalate monomers both serve to hinder the movement of protons within the lattice, resulting in longer off times. The reformation of a hydrogen bond between the oxygen atom in the lactone ring and neighboring phthalate monomer promotes the facile conversion of  $\text{VR}^{\text{L}}$  to  $\text{VR}^-$  such that the rate of proton tunneling is the rate-limiting step for  $\text{VR}^-$  formation and dictates the duration of the nonemissive states evident in the PI data.

**Log-Normal PDFs and Proton Transfer.** It is surprising that the PI of VR is poorly described by a power-law, but is instead consistent with a log-normal PDF. What are the implications of a log-normal PDF regarding proton transfer? Most hypotheses for PI involve Markovian processes where the future state of the system is independent of prior states that were populated. However, there are many reports of non-Markovian emission statistics including VR in KAP where a correlation of adjacent emissive and nonemissive event durations, commonly referred to as “memory”, is observed.<sup>10,41,49–54</sup> Interestingly, the log-normal distribution arises from processes characterized by memory.<sup>29</sup> The defining characteristic of a log-normal distribution is that the logarithm of the observations described by a given data set,  $\{X_0, X_1, \dots, X_i\}$ , are Gaussian distributed. The better known Gaussian distribution arises from the additive effect of many small random variations. Brownian diffusion results from the addition of random small movements caused by the interaction of a particle with the surrounding solvent. At the end of the observation time and after many particle movements, the probability of finding the particle at a given distance from the origin is Gaussian distributed. Physical phenomena demonstrating Gaussian statistics arise from the additive contribution of an underlying random process expressed as:

$$X_i = X_{i-1} + \epsilon_i \quad (12)$$

In the above expression,  $\epsilon_i$  are independent and identically distributed random numbers (that is, they have the same mean and standard deviation) such that they obey the central limit theorem (in the limit of a large number of samples ( $n$ ) the variable  $(\sum_i^n \epsilon_i)/n - \bar{\epsilon}$  is Gaussian distributed, where  $\bar{\epsilon}$  is the best estimate of the true mean). From the previous expression, the following can be derived:

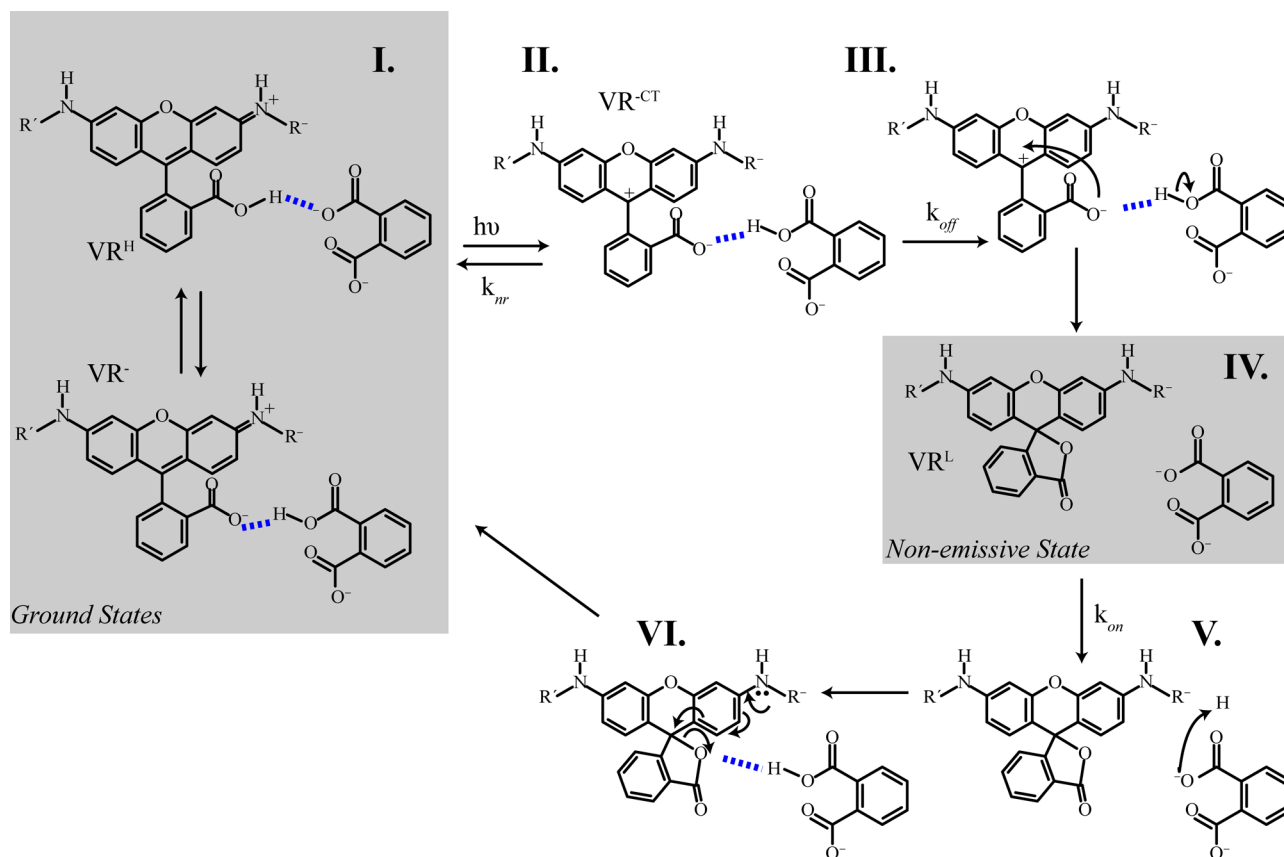


**Figure 12.** Proposed mechanism for PI of VR in KAP and DKAP. Detailed description of the mechanism is provided in the text.

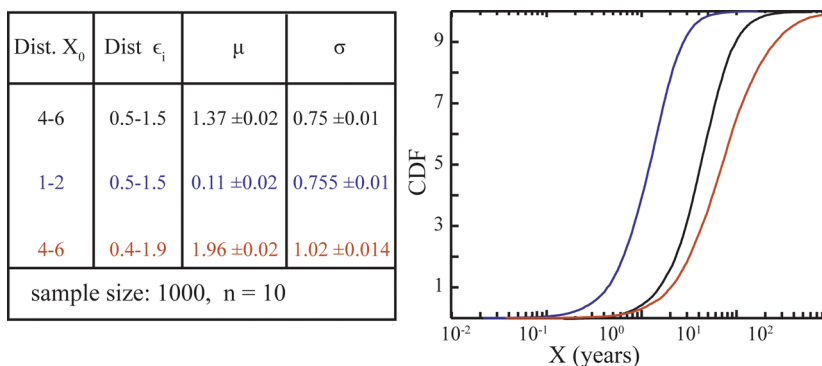


**Figure 13.** CDFs from simulated data of employee service distributions, where each of 1000 people in each group held 10 jobs. The distributions of  $X_0$  and  $\epsilon_i$  are uniformly distributed random numbers in the intervals given in the table. Changes in  $X_0$  result in changes in  $\mu$  but not  $\sigma$ . Changes in  $\epsilon_i$  result in changes in both log-normal parameters.

$$X_n = X_0 + \sum_{i=1}^n \epsilon_i \quad (13)$$

This expression demonstrates the *additive* effects of the random process on the observable of interest. In contrast, the log-normal distribution results from the proportionate contribution of the random process expressed as

$$X_i = X_{i-1} \epsilon_i \quad (14)$$

and, correspondingly,

$$X_n = X_0 \prod_{i=1}^n \epsilon_i \quad (15)$$

That is, for log-normal distributions the random variable has a *multiplicative* effect on the observable of interest. Taking the logarithm, the above expression becomes

$$\ln(X_n) = \ln(X_0) + \sum_{i=1}^n \ln(\epsilon_i) \quad (16)$$

In comparison to the Gaussian case above, one can see that as long as the central limit theorem applies to the logarithm of  $\epsilon_i$ , and the mean of  $\ln(\epsilon_i)$  is close to zero, then  $\ln(X_n)$  will be Gaussian.<sup>29,55,56</sup>

An illustration of the origin of log-normal distributions is the length of service for employees.<sup>57</sup> One variable characterizing an applicant is the duration of employment in prior positions.

The expectation is that the time an applicant will remain in their new position will be some multiple of the duration of previous employment. In addition to employment durations varying between individuals, length-of-employment distributions will also vary with field of employment (retail has higher turnover than engineering). Differences in employment durations for individuals is reflected by  $\sigma$  (the distribution width), where distributions for different employment fields will vary in  $\mu$  (the distribution median). To explore how a given distribution of starting conditions,  $X_0$ , and the distribution of random variability ( $\epsilon_i$ ) lead to the log-normal distribution for this employment example, we performed the following simulation. Three groups of 1000 people were poled after having 10 jobs each ( $n$ ). Two groups held their first job ( $X_0$ ) 2–4 years, and one group held their first job 1–2 years. The first two groups were subject to the same uniform random distribution ( $\epsilon_i$ ) on the interval [0.5–1.5], the third group had a distribution between [0.4–1.9]. The results of this simulation are provided in Figure 13. When the distribution of  $X_0$  is changed, the median ( $\mu$ ) of the resulting log-normal distribution changes but not  $\sigma$ . When the distribution of  $\epsilon_i$  changes, both parameters  $\mu$  and  $\sigma$  change. Therefore, for employees of all fields the first job experience leads to the differences in length of service distributions. Differences in  $\sigma$  between data sets collected under different environmental conditions can be interpreted to mean the underlying random process has also changed.

This description of a log-normal distribution helps when interpreting the variation in the *off*-interval CDFs with temperature. The *off*-interval CDFs in DKAP shift to longer times as the temperature is increased reflecting a change in  $\mu$  of the underlying log-normal PDF (Table 2). Furthermore, for both *on*- and *off*-intervals little variation in  $\sigma$  is observed. This suggests that at all three temperatures, VR is subjected to the same underlying random process (distribution of  $\epsilon_i$ ) and that the initial state of the system ( $X_0$ ) is altered. Connecting this to the proposed mechanism for dark-state production and decay, the parameter  $\mu$  reflects the proton mobility in KAP which changes with increased lattice spacing upon heating as well as the hydrogen bond length between VR and the neighboring phthalate. Random variability in proton conductivity (for example, variability connected to phonons) is contained in  $\sigma$ . Given the similarity of the values of  $\sigma$  in Table 2, we expect that dispersion of proton transfer rates remain the same.

The proportionality between successive *on*-intervals in KAP was investigated using log-normal PDFs as described above. A highly log-normal distribution with parameters of  $\mu = -0.02$  and  $\sigma = 2$  of was obtained for the “distribution of  $\epsilon_i$ ”. The value of  $\mu$  being close to zero suggests that the probability of subsequent intervals becoming shorter or longer is equivalent throughout the experiment. This distribution was not able to reproduce the blinking data most likely due to the random process causing intermittency on a time scale much shorter than the intervals themselves. In this limit, one should see only a modest correlation between interval durations, an expectation consistent with previous studies of VR in KAP.<sup>10</sup> Future modeling of log-normal time-series processes may provide further insight into PI,<sup>58</sup> narrowing possible distributions for the underlying random fluctuations that promote the intermittent phenomenon observed for single molecules.

## CONCLUSIONS

We have performed isotopic substitution experiments to evaluate the role of proton transfer in the PI exhibited by VR isolated in KAP and DKAP crystals. Statistically significant differences were observed for the distribution of *on*- and *off*-interval durations in the isotopomeric crystals supporting the proton-transfer model for PI. At room temperature, distributions of both *on*- and *off*-intervals were found to be statistically different between KAP and DKAP, as evidenced by  $p$ -values  $\ll 0.05$ . SM emission energies of both  $\text{VR}^-$  and  $\text{VR}^{\text{H}}$  further support the proton-transfer model. The *on*-interval distributions become statistically equivalent at elevated temperatures, whereas the *off*-intervals remain statistically different. This was interpreted as evidence for different proton-transfer mechanisms for dark state production and decay. We have proposed that formation of the colorless isomer,  $\text{VR}^{\text{L}}$ , is responsible for the nonemissive events observed in the PI data. Opening of the lactone ring corresponding to the conversion of  $\text{VR}^{\text{L}}$  to  $\text{VR}^-$  is mediated by proton-tunneling. Evidence of this mechanism is found in the temperature evolution of the *off*-intervals, where the average duration increases with increasing temperature consistent with an increase in the tunneling barrier accompanying expansion of the crystal lattice.

The *on*- and *off*-intervals are not consistent with a power-law distribution as previously assumed and are instead well modeled by a log-normal distribution. The observation of a log-normal distribution implies that the PI exhibited by VR in KAP arises from the multiplicative influence of a random process. Our data suggest that the differences among distributions is mostly the result of the initial state of the system (temperature and crystallographic dimensions), and that the underlying variability (distribution in proton hopping rates in KAP) giving rise to the log-normal demonstrates little variation in *on*- and *off*-intervals.

## ASSOCIATED CONTENT

### Supporting Information

Crystallographic information files (CIF) for potassium hydrogen phthalate (KAP) and potassium deuterium phthalate (DKAP) for temperatures 20 and 87 °C. This material is available free of charge via the Internet at <http://pubs.acs.org>.

## AUTHOR INFORMATION

### Corresponding Author

\*E-mail: [bart.kahr@nyu.edu](mailto:bart.kahr@nyu.edu); [preid@chem.washington.edu](mailto:preid@chem.washington.edu).

### Notes

The authors declare no competing financial interest.

## ACKNOWLEDGMENTS

B.K. thanks the National Science Foundation (CHE-08545526, DMR-1105000). P.J.R. thanks the National Science Foundation (DMR-1005819).

## REFERENCES

- (1) Kulzer, F.; Xia, T.; Orrit, M. *Angew. Chem., Int. Ed.* **2010**, *49*, 854–866.
- (2) Schulman, J. H.; Compton, W. D. *Color Centers in Solids*; The MacMillan Company: New York, 1962.
- (3) Kahr, B.; Gurney, R. W. *Chem. Rev.* **2001**, *101*, 893–951.
- (4) Wustholz, K. L.; Sluss, D. R. B.; Kahr, B.; Reid, P. J. *Int. Rev. Phys. Chem.* **2008**, *27*, 167–200.



- (5) Barbon, A.; Bott, E. D.; Brustolon, M.; Fabris, M.; Kahr, B.; Kaminsky, W.; Reid, P. J.; Wong, S. M.; Wustholz, K. L.; Zanre, R. J. *Am. Chem. Soc.* **2009**, *131*, 11548–11557.
- (6) Wustholz, K. L.; Kahr, B.; Reid, P. J. *J. Phys. Chem. B* **2005**, *109*, 16357–16362.
- (7) Wustholz, K. L.; Bott, E. D.; Isborn, C. M.; Li, X.; Kahr, B.; Reid, P. J. *J. Phys. Chem. C* **2007**, *111*, 9146–9156.
- (8) Riley, E. A.; Bingham, C.; Bott, E. D.; Kahr, B.; Reid, P. J. *J. Phys. Chem. Phys.* **2011**, *13*, 1879–1887.
- (9) Riley, E. A.; Hess, C. M.; Whitham, P. J.; Reid, P. J. *J. Chem. Phys.* **2012**, *136*, 184508–10.
- (10) Wustholz, K. L.; Bott, E. D.; Kahr, B.; Reid, P. J. *J. Phys. Chem. C* **2008**, *112*, 7877–7885.
- (11) Tredwell, C. J.; Osborne, A. D. *J. Chem. Soc., Faraday Trans. 2* **1980**, *76*, 1627–1637.
- (12) Bruker APEX2 (version 2.1–4), SAINT (version 7.34A), SADABS (version 2007/4); BrukerAXS Inc: Madison, Wisconsin, USA, 2007.
- (13) Altomare, A.; Burla, M. C.; Camalli, M.; Cascarano, G. L.; Giacovazzo, C.; Guagliardi, A.; Moliterni, A. G. G.; Polidori, G.; Spagna, R. *J. Appl. Crystallogr.* **1999**, *32*, 115–119.
- (14) Altomare, A.; Cascarano, G.; Giacovazzo, C.; Guagliardi, A. J. *J. Appl. Crystallogr.* **1993**, *26*, 343–350.
- (15) Sheldrick, G. M. *SHELXL-97*, Program for the Refinement of Crystal Structures; University of Göttingen: Germany, 1997.
- (16) Mackay, S. E., C.; Henderson, A.; Gilmore, C.; Stewart, N.; Shankland, K.; Donald, A. *MaXus*, a computer program for the solution and refinement of crystal structures from diffraction data; University of Glasgow: Scotland, 1997.
- (17) Waasmaier, D.; Kirfel, A. *Acta Crystallogr., Sect. A* **1995**, *51*, 416–431.
- (18) Watkins, L. P.; Yang, H. J. *J. Phys. Chem. B* **2005**, *109*, 617–628.
- (19) Arbeloa, F. L.; Arbeloa, T. L.; Estevez, M. J. T.; Arbeloa, I. L. *J. Phys. Chem.* **1991**, *95*, 2203–2208.
- (20) Arbeloa, T. L.; Arbeloa, F. L.; Bartolome, P. H.; Arbeloa, I. L. *Chem. Phys.* **1992**, *160*, 123–130.
- (21) Karpiuk, J.; Grabowski, Z. R.; Deschryver, F. C. *J. Phys. Chem.* **1994**, *98*, 3247–3256.
- (22) Osborne, A. D.; Winkworth, A. C. *Chem. Phys. Lett.* **1982**, *85*, 513–517.
- (23) Bullard, T.; Wustholz, K. L.; Bott, E. D.; Robertson, M.; Reid, P. J.; Kahr, B. *Cryst. Growth Des.* **2009**, *9*, 982–990.
- (24) Mohan Kumar, R.; Rajan Babu, D.; Murugakoothan, P.; Jayavel, R. *J. Cryst. Growth* **2002**, *245*, 297–303.
- (25) Kuno, M.; Fromm, D. P.; Hamann, H. F.; Gallagher, A.; Nesbitt, D. J. *J. Chem. Phys.* **2001**, *115*, 1028–1040.
- (26) Hoogenboom, J. P.; den Otter, W. K.; Offerhaus, H. L. *J. Chem. Phys.* **2006**, *125*, 204713.
- (27) Clauset, A.; Shalizi, C. R.; Newman, M. E. J. *SIAM Rev.* **2009**, *51*, 661–703.
- (28) Press, W. H.; Teukolsky, S. A.; Vetterling, W. T.; Flannery, B. P. *Numerical Recipes: The Art of Scientific Computing*, 3rd ed.; Cambridge University Press: Cambridge, 2007.
- (29) Crow, E. L.; Shimizu, K. *Lognormal Distributions: Theory and Applications*; M. Dekker: New York, 1988.
- (30) Ye, M.; Searson, P. C. *Phys. Rev. B* **2011**, *84*, 125317.
- (31) Cichos, F.; von Borczyskowski, C.; Orrit, M. *Curr. Opin. Colloid Interface Sci.* **2007**, *12*, 272–284.
- (32) Tang, J.; Marcus, R. A. *J. Chin. Chem. Soc.* **2006**, *53*, 1–13.
- (33) Kruger, T. P. J.; Illoia, C.; Valkunas, L.; van Grondelle, R. *J. Phys. Chem. B* **2011**, *115*, 5083–5095.
- (34) Lee, J.-E.; Yang, J.; Kim, D. *Faraday Discuss.* **2012**, *155*, 277–288.
- (35) Hofkens, J.; Vosch, T.; Maus, M.; Kohn, F.; Cotlet, M.; Weil, T.; Herrmann, A.; Mullen, K.; De Schryver, F. C. *Chem. Phys. Lett.* **2001**, *333*, 255–263.
- (36) Neuhauser, R. G.; Shimizu, K. T.; Woo, W. K.; Empedocles, S. A.; Bawendi, M. G. *Phys. Rev. Lett.* **2000**, *85*, 3301–3304.
- (37) Plakhotnik, T.; Fernée, M. J.; Littleton, B.; Rubinsztein-Dunlop, H.; Potzner, C.; Mulvaney, P. *Phys. Rev. Lett.* **2010**, *105*, 167402.
- (38) Stracke, F.; Blum, C.; Becker, S.; Müllen, K.; Meixner, A. *J. ChemPhysChem* **2005**, *6*, 1242–1246.
- (39) Bott, E. D.; Riley, E. A.; Kahr, B.; Reid, P. J. *ACS Nano* **2009**, *3*, 2403–2411.
- (40) Andresen, M.; Stiel, A. C.; Trowitzsch, S.; Weber, G.; Eggeling, C.; Wahl, M. C.; Hell, S. W.; Jakobs, S. *Proc. Natl. Acad. Sci. U.S.A.* **2007**, *104*, 13005–13009.
- (41) Fukaminato, T. *J. Photochem. Photobiol., C* **2011**, *12*, 177–208.
- (42) Vogelsang, J.; Steinhauer, C.; Forthmann, C.; Stein, I. H.; Person-Skegro, B.; Cordes, T.; Tinnefeld, P. *ChemPhysChem* **2010**, *11*, 2475–2490.
- (43) Haase, M.; Hübner, C. G.; Nolde, F.; Müllen, K.; Basché, T. *Phys. Chem. Chem. Phys.* **2011**, *13*, 1776–1785.
- (44) Sluss, D.; Bingham, C.; Burr, M.; Bott, E. D.; Riley, E. A.; Reid, P. J. *J. Mater. Chem.* **2009**, *19*, 7561–7566.
- (45) Vogelsang, J.; Kasper, R.; Steinhauer, C.; Person, B.; Heilemann, M.; Sauer, M.; Tinnefeld, P. *Angew. Chem., Int. Ed.* **2008**, *47*, 5465–5469.
- (46) Yeow, E. K. L.; Melnikov, S. M.; Bell, T. D. M.; De Schryver, F. C.; Hofkens, J. *J. Phys. Chem. A* **2006**, *110*, 1726–1734.
- (47) Varma, K. B. R. *Cryst. Res. Technol.* **1988**, *23*, 185–193.
- (48) Miyoshi, T.; Mashiyama, H.; Asahi, T.; Kimura, H.; Noda, Y. *J. Phys. Soc. Jpn.* **2011**, *80*, 044709.
- (49) Hoogenboom, J. P.; Hernando, J.; García-Parajó, M. F.; van Hulst, N. F. *J. Phys. Chem. C* **2008**, *112*, 3417–3422.
- (50) Stefani, F. D.; Zhong, X. H.; Knoll, W.; Han, M. Y.; Kreiter, M. *New J. Phys.* **2005**, *7*, 197.
- (51) Yang, S. L.; Cao, J. S. *J. Chem. Phys.* **2002**, *117*, 10996–11009.
- (52) Cakir, R.; Grigolini, P.; Krokchin, A. A. *Phys. Rev. E: Stat., Nonlinear, Soft Matter Phys.* **2006**, *74*, 021108.
- (53) Volkán-Kacsó, S.; Frantsuzov, P. A.; Jankó, B. *Nano Lett.* **2010**, *10*, 2761–2765.
- (54) Lee, J. D.; Maenosono, S. *Phys. Rev. B: Condens. Matter Mater. Phys.* **2009**, *80*, 205327.
- (55) Koch, A. L. *J. Theor. Biol.* **1966**, *12*, 276–290.
- (56) Limpert, E.; Stahel, W. A.; Abbt, M. *Bioscience* **2001**, *51*, 341–352.
- (57) Bartholomew, D. J. *Stochastic Models for Social Processes*; Wiley: London; New York, 1973.
- (58) Perpete, N.; Schmitt, F. G. *J. Stat. Mech.* **2011**, P12013.